Radiation driving and heating of general relativistic jets under a Compton-scattering regime

Mukesh K. Vyas★ and Indranil Chattopadhyay★
Aryabhatta Research Institute of Observational Sciences (ARIES), Manora Peak, Nainital 263002, India

ABSTRACT

Interaction of intense radiation from the underlying accretion disc with a steady, general-relativistic jet is studied. The radiation field imparts momentum as well as energy to the outflowing jet under Compton scattering. As a result, the jet gains momentum and is simultaneously heated up. Jets can be classified as types A, B and C according to their base properties. We found that A-type jets can undergo shock transition. It is also shown that, in the Compton-scattering regime, radiation can drive jets starting with very small thermal energy at the base (B- and C-type jets), such that radiation can even accelerate bound matter (generalized Bernoulli parameter $E < 1$) in the form of relativistic transonic jets. This is in stark contrast to radiatively driven jets in the Thomson-scattering regime, where transonic jets were obtained only for $E > 1$. We also show that, for a given disc luminosity, jets in the Compton-scattering regime exhibit a minimum terminal speed, unlike in the Thomson-scattering domain. Further, the impact of accretion-disc luminosity and jet plasma composition is studied. The $e^- - p^+$ jets are accelerated up to Lorentz factors of about a few, while for lepton-dominated jets the minimum Lorentz factor exceeds 10 for moderate disc luminosities and can go up to a few tens for highly luminous discs.

Key words: radiation: dynamics – scattering – shock waves – stars: black holes – ISM: jets and outflows.

1 INTRODUCTION

Astrophysical jets were first discovered by Curtis ([1918](#)) at optical wavelengths while studying M87. After the advent of radio astronomy, these jets were studied in detail in the later half of the 19th century. Since then, the jets have been recognized as ubiquitous astrophysical phenomena associated with various classes of objects like active galactic nuclei (AGN: e.g. M87, 3C 279), young stellar objects (YSOs: e.g. HH 30, HH 34) and X-ray binaries (e.g. SS433, Cyg X-3, GRS 1915 + 105, GRO 1655-40). In black hole (BH) sources, jets can only emerge from accreting matter, because BHs are not capable of emitting matter or radiation. The strong correlation observed between spectral states of accretion discs and jet evolution (Gallo, Fender & Pooley [2003](#); Fender, Gallo & Russell [2010](#); Rushton et al. [2010](#)) suggests that the jets are launched by the disc. Further, jets were observed to be launched from a region within a few tens of Schwarzschild radii (r_s) from the central BH (Junor, Biretta & Livio [1999](#); Doeleman et al. [2012](#)). Hence jets are generated from the hot and more active inner region of the accretion disc. These facts make it important to study the impact of thermal pressure, as well as the radiation field, on the dynamics of the jet.

Along with the development of various accretion disc models (Shakura & Sunyaev [1973](#); Paczyński & Wiita [1980](#); Fukue [1987](#); Chakrabarti [1989](#); Narayan, Kato & Honma [1997](#)), several attempts were made to understand the interaction of radiation from these discs with outflowing jets. In this article, the jets are studied in the radiation hydrodynamic (RHD) regime. The RHD equations of motion (EoM) were developed by various authors in the special relativistic or SR regime (Hsieh & Spiegel [1976](#); Calvini & Nobili [1982](#); Mihalas & Mihalas [1984](#); Kato, Fukue & Mineshige [1998](#)) and in the general relativistic (GR) regime (Park [2006](#); Takahashi [2007](#)).

Significant development of the field started from the 1980s. Sikora & Wilson ([1981](#)) studied particle jets driven by radiation in the SR regime. Odell ([1981](#)) showed that the Thomson-scattering radiation force increases for hot plasma, which might result in enhanced radiative driving called the 'Compton rocket'. However, Phinney ([1982](#)) downplayed the significance of the Compton rocket in the presence of Compton cooling. Ferrari et al. ([1985](#)) studied radiatively driven fluid jets in the SR regime. They considered Newtonian gravitational potential, along with an isothermal equation of state (EoS), with which they produced mildly relativistic jets and obtained internal shocks as a manifestation of the jet geometry. Icke ([1989](#)) studied the role of radiation drag on particle jets plying through the radiation field produced by an infinite Keplerian disc.

★ E-mail: mukesh.vyas@aries.res.in (MKV); indra@aries.res.in (IC)

He discovered the upper limit of the speed of matter to be $0.45c$, where c is the speed of light in vacuum. Fukue (1996) studied particle jets under a radiation field, considering a pseudo-Newtonian potential (pNp) to take care of strong gravity. Fukue, Tojyo & Hirai (2001) considered a hybrid disc and produced jets with $\gamma_T \sim 2$.

Through various numerical (Molteni, Ryu & Chakrabarti 1996; Das et al. 2014; Lee et al. 2016) and theoretical studies (Chattopadhyay & Das 2007; Kumar & Chattopadhyay 2013, 2017; Kumar et al. 2013; Kumar, Chattopadhyay & Mandal 2014; Chattopadhyay & Kumar 2016), it was found that an extrathermal gradient force in the corona close to the BH automatically generates bipolar outflows. Driving of jets by radiation from an advective disc was also investigated (Chattopadhyay & Chakrabarti 2000a,b, 2002a,b). In the non-relativistic regime, the formalism followed by Chattopadhyay & Chakrabarti (2000a, 2002a) is only correct up to the first order of the flow velocity. Full relativistic transformations of radiative moments were later considered and implemented for particle jets in the SR regime (Chattopadhyay, Das & Chakrabarti 2004; Chattopadhyay 2005). The disc chosen was of the hybrid type with two sources of radiation: (i) the Keplerian disc and (ii) the post-shock region of the sub-Keplerian component of the disc. These authors also showed that relativistic jets ($\gamma_T \gtrsim 2$) with impressive collimation could be achieved for such jets.

Most of the above cited studies were conducted either in the particle regime, i.e. the gas pressure was neglected compared with the radiation pressure, or by considering fluids in the non-relativistic regime. Vyas et al. (2015, hereafter VKMC15) solved the RHD equations of motion for jets described by a relativistic EoS. The authors considered special relativistic space–time and the gravity was mimicked by a pNp that was initially proposed by Paczyński & Wiita (1980). It is well known that, for hot flows, radiation driving becomes ineffective and yet VKMC15 showed that jets can be accelerated to relativistic terminal speeds. The strong temperature gradient drives the jet just above the base and thereafter radiation driving takes over. In fact, the thermal driving is so strong that it accelerates the jet to a speed of about 10 per cent of the speed of light within the first few Schwarzschild radii above the disc. In this region, the radiation field actually decelerates the jet, due to an effect called radiation drag, beyond which the jet is accelerated by the radiation field.

There were two limitations of VKMC15: (i) combining SR with a gravitational potential and (ii) consideration of conical flow geometry. We addressed these two issues separately in a general relativistic analysis. We showed the formation of moderately strong internal shocks to be a direct fallout of non-conical geometry (Vyas & Chattopadhyay 2017, hereafter VC17) and then radiation driving of jets in curved geometry was considered for flow described by a fixed adiabatic index (Γ) EoS (Vyas & Chattopadhyay 2018a), as well as with a relativistic EoS (Vyas & Chattopadhyay 2018b, hereafter VC18b). We showed that considering jets in the SR regime with an ad hoc gravitational potential produces unphysically hot flow, producing an additional thermal gradient push. In other words, because jets are supposed to be launched close to the compact object, consideration of GR is important.

To simplify the analysis in most of the works cited above, the interaction of disc radiation with jet matter was considered in the elastic scattering regime. Under this assumption, the radiation field only transfers momentum to the jet, but there is no energy transfer between them. If the radiation is of the order of $\lesssim$ few $\times$ 10 KeV, then an elastic scattering cross-section (i.e. Thomson-scattering cross-section) is applicable, but if higher energy photons impinge on electrons then a Thomson-scattering cross-section is untenable. There

were very few studies on Compton-driving of outflows. Quinn & Paczynski (1985) and Turolla, Nobili & Calvani (1986) considered radiatively driven winds accompanied by an energy exchange between radiation and matter, mostly in the optically thick regime. There was initial apprehension about 'a severe' limit on driving a jet in the optically thin regime because of the presence of radiation drag (Icke 1989); however, later it was shown by a number of authors that if the bulk of intense radiation comes from the inner part of the accretion disc, radiation drag ceases to be a major obstacle for jet driving (Chattopadhyay et al. 2004; Chattopadhyay 2005) at a distance of about 100 Schwarzschild radii above the disc plane. At such distances, the radiation field remains significant enough to drive the jet matter.

In the current article, we consider radiatively driven jets in curved space–time using a general scattering cross-section (Buchler & Yueh 1976; Paczyński 1983), which enables energy as well as momentum transfer from radiation to the jet matter. The thermodynamics of the jet material is described by a relativistic EoS (Chattopadhyay 2008; Chattopadhyay & Ryu 2009) and the radiation moments were computed by considering the effects of space–time curvature (Beloborodov 2002). In the elastic scattering regime (VC18b), the radiatively driven jet solutions were primarily of two types: (i) jets launched with a hot base and higher speeds and (ii) jets launched with a moderately hot base but with almost negligible base speeds. The second type of solution is due to the geometrically thick corona. In this article, the height of the inner corona is adopted from Kato et al. (1998) and the corona height cannot increase beyond a limit. Therefore, it is indeed intriguing to find out how the jet solutions would change in light of the two modifications considered, namely Compton-scattering cross-section and modified corona size. VC18b also obtained radiatively driven internal shocks. Do such solutions survive in the Compton regime? How would the jet solutions be modified if the composition of the flow is varied? These are some of the questions that are discussed in this article.

In the next section, we present detailed mathematical formalism including the EoM and estimation of the radiation field. We then briefly discuss our methods of obtaining results in Section 3. We describe the results of the study in Section 4 and conclude the article in Section 5. A description of the relativistic EoS used is given in Appendix A, while the detailed method of calculating the radiation field is given in Appendix B.

2 MATHEMATICAL FORMALISM

2.1 Space–time metric, unit system and assumptions made in the study

We consider a non-rotating black hole described by a Schwarzschild metric:

$$
\begin{aligned}
ds^2 &= -g_{tt}c^2\,dt^2 + g_{rr}\,dr^2 + g_{\theta\theta}\,d\theta^2 + g_{\phi\phi}\,d\phi^2 \\
&= -\left(1 - \frac{2GM_B}{c^2 r}\right)c^2\,dt^2 + \left(1 - \frac{2GM_B}{c^2 r}\right)^{-1} dr^2 \\
&\quad + r^2\,d\theta^2 + r^2\sin^2\theta\,d\phi^2.
\end{aligned}
\tag{1}
$$

Here, r, θ, ϕ and t are space–time coordinates. M_B and G are the BH mass and the universal constant of gravitation, respectively. In this article, we have used geometric units $G = M_B = c = 1$, such that the event horizon or Schwarzschild radius is $r_S = 2$. The jet is assumed to be around the axis of symmetry of the underlying accretion disc. The jet is stationary and axisymmetric (i.e. $\partial/\partial t = \partial/\partial\phi = 0$). Since jets are collimated, we consider the jet to be conical (i.e.
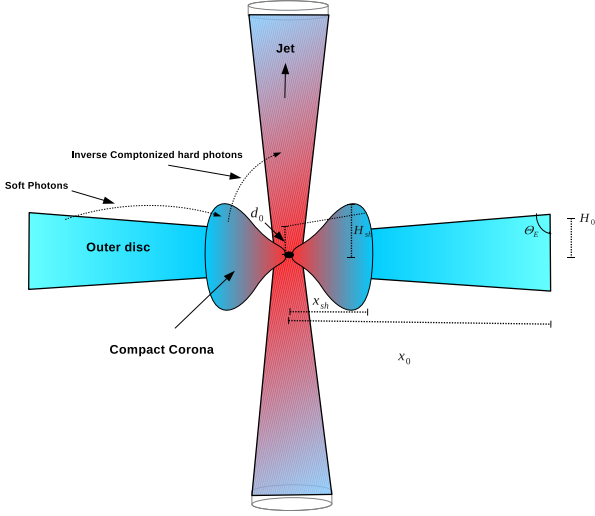
Figure 1. Cartoon diagram of the disc–jet system. The outer extent and height of the corona x_{sh} and H_{sh}, intercept of the outer disc on the axis (d_0) and outer edge of the disc x_0 are shown. The funnel of the corona is also shown.

cross-section $\mathcal{A} \propto r^2$) with a narrow opening angle. In this article, we do not consider the exact launching mechanism of jets from the accretion disc: instead, the accretion disc acts only as the source of radiation. The accretion disc is around the equatorial plane. The inner part of the accretion disc has a geometrically thick corona and the expression for the height of the corona (H_{sh}) is given as (Kato et al. 1998)

$$H_{sh} = H^* \left(1 - \sqrt{\frac{2}{x_{sh}}} \right). \tag{2}$$

Here H^* and x_{sh} are upper limit of the corona height and horizontal extent of the corona, respectively. The expression for the corona cross-section is different from VC18b, where the corona was assumed to be thick. In the current article, if the horizontal extent of the corona is large, then the corona is geometrically slim (H_{sh}/x_{sh} < 1). A typical cartoon diagram of the assumed system is given in Fig. 1, which shows a bipolar radial jet coming out of a nearby region inside the coronal funnel. The outer portion of the disc is also shown. The cartoon of the disc–jet system presupposes the jet is launched from the inner part of the disc, although not explicitly computed from first principles.

2.2 Radiation hydrodynamic equations governing the dynamics of relativistic fluids

The energy–momentum tensors for matter ($T_M^{\mu\nu}$) and radiation ($T_R^{\mu\nu}$) are given by

$$T^{\mu\nu} = T_M^{\mu\nu} + T_R^{\mu\nu},$$

where

$$T_M^{\mu\nu} = (e + p)u^\mu u^\nu + pg^{\mu\nu}$$

and

$$T_R^{\mu\nu} = \int I l^\mu l^\nu \, d\Omega. \tag{3}$$

Here, u^μ are the components of four-velocity, l^μ are directional derivatives, I is the frequency-integrated specific intensity of the radiation field and $d\Omega$ is the differential solid angle subtended by

a source point on the accretion-disc surface with reference to the field point on the jet axis. The assumption of conical outflow along the axis of symmetry of the accretion disc implies that the only significant component of four-velocity is u^r.

The equations of motion are given by

$$T^{\mu\nu}_{;\nu} = 0 \quad \text{and} \quad (\rho u^\nu)_{;\nu} = 0. \tag{4}$$

The momentum-balance equation obtained under the present set of assumptions is along the radial direction:

$$u^r \frac{du^r}{dr} + \frac{1}{r^2} = -\left(1 - \frac{2}{r} + u^r u^r \right) \frac{1}{e+p} \frac{dp}{dr} + \rho_e \frac{\sqrt{g^{rr}}\gamma^3}{(e+p)} \Im^r. \tag{5}$$

Here, $\gamma = -u_t u^t = (1-v^2)^{-1/2}$ is the bulk Lorentz factor of the jet, where $v = \sqrt{(-u_r u^r/u_t u^t)}$ is the three-velocity in the radial direction. This means that $u^r = \sqrt{g^{rr}}\gamma v$. The total lepton mass density is given by ρ_e and $\Im^r$ is the momentum imparted to the jet plasma by the radiation field of the accretion disc, which is given by

$$\Im^r = \frac{\sigma}{m_e} \left[(1+v^2)\mathcal{R}_1 - v \left(g^{rr}\mathcal{R}_0 + \frac{\mathcal{R}_2}{g^{rr}} \right) \right]. \tag{6}$$

The first three moments of the specific intensity of the radiation field are $\mathcal{R}_0$, $\mathcal{R}_1$ and $\mathcal{R}_2$ and are identified as the radiation energy density, flux and pressure, respectively. However, similarly to VC18b, we refer to $R_0 = \sigma_T \mathcal{R}_0/(m_e)$, $R_1 = \sigma_T \mathcal{R}_1/(m_e)$ and $R_2 = \sigma_T \mathcal{R}_2/(m_e)$ as the respective radiative moments. The detailed method of estimation of radiative moments is given in Appendix B (see also VC18b). The negative terms arise for an optically thin medium and as long as the jet 'sees' the accretion disc as an extended radiator. These negative terms are called 'radiation drag' terms; they arise because of the anisotropic nature of the radiation field and are stronger near the disc surface. The scattering cross-section σ is given as (Buchler & Yueh 1976; Paczyński 1983)

$$\sigma = \chi_c \sigma_T = \left[\frac{1}{1 + \left(\frac{T_e}{4.5 \times 10^8} \right)^{0.86}} \right] \sigma_T, \tag{7}$$

where, σ_T is the Thomson scattering cross-section. χ_c accounts for Compton processes (i.e. energy exchange between radiation and matter) and is <1. T_e is the electron temperature in physical units. It is approximated as a function of N (Kumar & Chattopadhyay 2014; Singh & Chattopadhyay 2018):

$$\Theta_e = \frac{kT_e}{m_e c^2} = -\frac{2}{3} + \frac{1}{3}\sqrt{\left[4 - 2\left(\frac{2N-3}{N-3} \right) \right]}.$$

Although the form of equation (5) is similar to the one in VC18b, the difference is in the expression for σ.

The first law of thermodynamics, or energy equation $\left(u_\alpha T_{M;\beta}^{\alpha\beta} = -u_\mu T_{R;\nu}^{\mu\nu} \right)$, is obtained as

$$\frac{de}{dr} - \frac{e+p}{\rho}\frac{d\rho}{dr} = -\frac{\gamma \rho_e (1-\chi_c) R_t}{\sqrt{g^{rr}}}. \tag{8}$$

Here R_t is the radiative contribution, representing energy exchange between the imparted radiation and the fluid (the same as the heating term of Park 2006):

$$R_t = \left[\frac{g^{rr} R_0}{v} + \frac{v R_2}{g^{rr}} - 2R_1 \right]. \tag{9}$$

Integrating the conservation of mass flux (the second part of equation 4), we obtain the mass outflow rate

$$\dot{M}_o = \rho u^r \mathcal{A}. \tag{10}$$

Here $\mathcal{A}$ is the cross-section of the jet. Since the jet is transonic and collimated, we assume the cross-section to be conical ($\mathcal{A} \propto r^2$). However, the radiation supplies energy to the jet and makes it hotter, which might raise the apprehension that the assumption of conical jet may not hold. We discuss this in greater detail in Section 5 and Appendix C and we show that the assumption is reasonable. In VC18b, the elastic scattering assumption rendered $R_t = 0$ and therefore, integrating equation (8) with the help of the EoS (equation A1), we obtained the adiabatic relation between Θ and ρ (Kumar et al. 2013). Replacing ρ of the adiabatic relation in equation (10), we also obtained the expression for the entropy-outflow rate (VKMC15; VC18b):

$$\dot{\mathcal{M}} = \exp(k_3)\Theta^{3/2}(3\Theta + 2)^{k_1}(3\Theta + 2/\eta)^{k_2}u^r\mathcal{A}, \quad (11)$$

where $k_1 = 3(2 - \xi)/4$, $k_2 = 3\xi/4$ and $k_3 = (f - \tau)/(2\Theta)$. This is also a measure of entropy of the jet and, unlike VKMC15 and VC18b, $\dot{\mathcal{M}}$ is not a constant in this article.

Integrating the first part of equation (4) is equivalent to integrating equations (5) and (8) simultaneously and we obtain the generalized, relativistic Bernoulli constant as the constant of motion:

$$E = -hu_t e^{-X_f},$$
$$\text{where}$$
$$X_f = \int dr \frac{\gamma(2 - \xi)}{(f + 2\Theta)\sqrt{g^{rr}}} \left[\Im^r - (1 - \chi_c)R_t\right]. \quad (12)$$

In the absence of radiation, this is merely $E = E_t = -hu_t$. With the help of equation (A2), equations (5) and (8) can be expressed as gradients of v and Θ and are given by

$$\gamma^2 v g^{rr} r^2 \left(1 - \frac{a^2}{v^2}\right)\frac{dv}{dr} = a^2\left(\frac{g^{rr}r^2}{\mathcal{A}}\frac{d\mathcal{A}}{dr} + 1\right) - 1$$
$$+ \frac{(2 - \xi)\gamma r^2\sqrt{g^{rr}}}{f + 2\Theta}\left[\Im^r - \frac{(1 - \chi_c)R_t}{N}\right] \quad (13)$$

and

$$\frac{d\Theta}{dr} = -\frac{\Theta}{N}\left[\frac{\gamma^2}{v}\left(\frac{dv}{dr}\right) + \frac{1}{\mathcal{A}}\frac{d\mathcal{A}}{dr} + \frac{1}{g^{rr}r^2} - \frac{(2-\xi)(1-\chi_c)\gamma R_t}{2\Theta\sqrt{g^{rr}}}\right]. \quad (14)$$

3 METHOD OF OBTAINING SOLUTIONS

Jet solutions are obtained by integrating equations (13) and (14). The jet base is close to the horizon. As the jet is hot and slow near the base, it is subsonic. In this article, the jet base is generally considered to be at $r = r_b = 3$ until otherwise specified. At large distances from the BH, the jet moves with very high speed and is cold and hence supersonic. In other words, the jets are transonic, i.e. the subsonic branch of the solution passes on to the supersonic one through the sonic point ($r = r_c$), i.e. at r_c, $v_c = a_c$. Here the suffix 'c' denotes quantities at the sonic point. Further, at r_c, $dv/dr \to 0/0$, which enables us to write down the other sonic-point condition as

$$\left[a^2\left(\frac{g^{rr}r^2}{\mathcal{A}}\frac{d\mathcal{A}}{dr} + 1\right) - 1 + \frac{(2-\xi)\gamma r^2\sqrt{g^{rr}}}{f + 2\Theta}\right.$$
$$\left. \times \left\{\Im^r - \frac{(1-\chi_c)R_t}{N}\right\}\right]_{r=r_c} = 0. \quad (15)$$

Here, $dv/dr|_c$ is calculated by employing L'Hospital's rule at r_c and solving the resulting quadratic equation for $dv/dr|_c$. The resulting quadratic equation can admit a complex root, leading to spiral-type sonic points, or two real roots. Solutions with two real roots but with
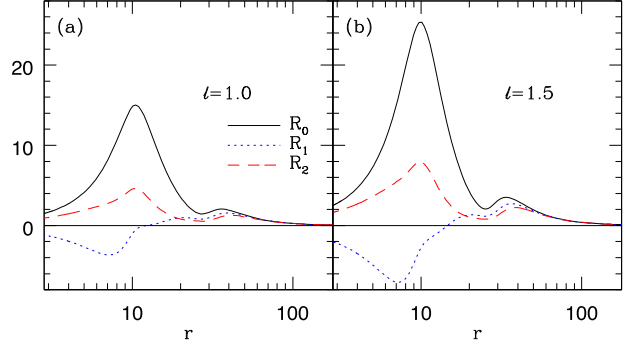

Figure 2. Distribution of radiative moments R_0 (solid), R_1 (dotted) and R_2 (dashed) for (a) $\ell = 1.0$ and (b) $\ell = 1.5$ along the jet length r.

opposite signs are called 'X' or 'saddle'-type sonic points, while real roots with the same sign produce a nodal-type sonic point. The jet solutions passing through X-type sonic points are physical so, for a given set of flow variables at the jet base, a unique solution will pass through the sonic point determined by the entropy $\dot{\mathcal{M}}$ of the flow. For given values of inner boundary condition, that is, at the jet base r_b, v_b and Θ_b, we integrate equations (13) and (14), while checking for the sonic-point conditions (equations 15). A set of r_b, $\sim v_b$ and Θ_b corresponds to a particular value of the constant of motion E. Various combinations of v_b and Θ_b can give rise to the same E, but only a particular value of $\dot{\mathcal{M}}$ corresponding to the same E will admit a sonic point and, following the second law of thermodynamics, $\dot{\mathcal{M}}$ of the transonic solution is maximum for all global solutions. We iterate till the sonic point is obtained and once it is obtained we continue to integrate outwards, starting from the sonic point using Runge–Kutta's fourth-order method. This process gives us values of v and Θ along r. All other variables, such as a, Γ, N, h, E_t and E, are obtained from these two variables. As explained in detail in VC18b, we check for shock transition by conserving fluxes at each point, namely mass flux, momentum flux and energy flux.

4 ANALYSIS AND RESULTS

4.1 Nature of the radiation field

We calculate radiative moments as explained in Appendix B. In Fig. 2, we show the intensity of the radiation field along r by plotting the radiative energy density R_0 (solid), r component of radiative flux R_1 (dotted) and rr component of radiative pressure R_2 (dashed) for various disc luminosities of the accretion disc, $\ell = 1.0$ and 1.5 in panels (a) and (b), respectively. These luminosities correspond to accretion rates $\dot{m} = 4.62$ and 4.89, respectively. The radiation field gets weaker as the luminosity decreases. Radiation flux R_1 is negative inside the funnel of the corona, which adds to the radiation drag term and resists the jet flow, while the flux is positive above the corona, hence it accelerates the jet, so radiation can accelerate or decelerate and also heats up the flow. We will explain these effects further in the next section.

4.2 Flow variables at sonic points

As shown before, sonic-point analysis is an important aspect of obtaining flow solutions, because at the sonic-point flow speed v equals sound speed a, which is essentially a mathematical boundary. Each sonic point corresponds to certain E or, equivalently, corre-
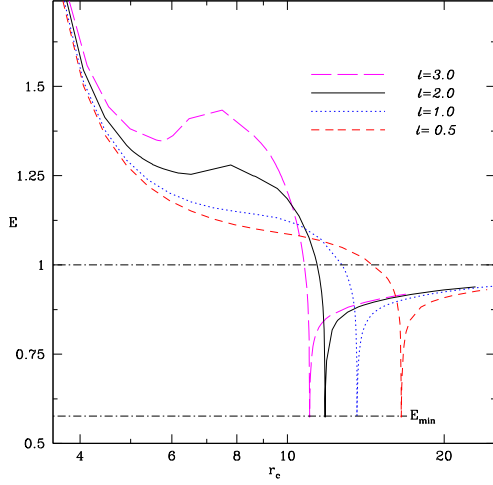
Figure 3. Variation of E with r_c for $\ell = 3.0$ (long-dashed) $\ell = 2.0$ (solid), $\ell = 1.0$ (dotted) and $\ell = 0.5$ (dashed).
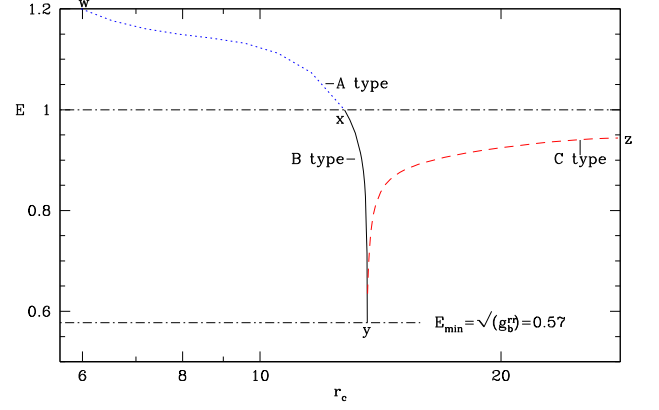

Figure 4. Variation of E with r_c for $\ell = 1.0$. Depending upon nature of the jet base, the solutions are classified into three types: A (dotted), B (solid) and C type (dashed). These are marked in the figure.
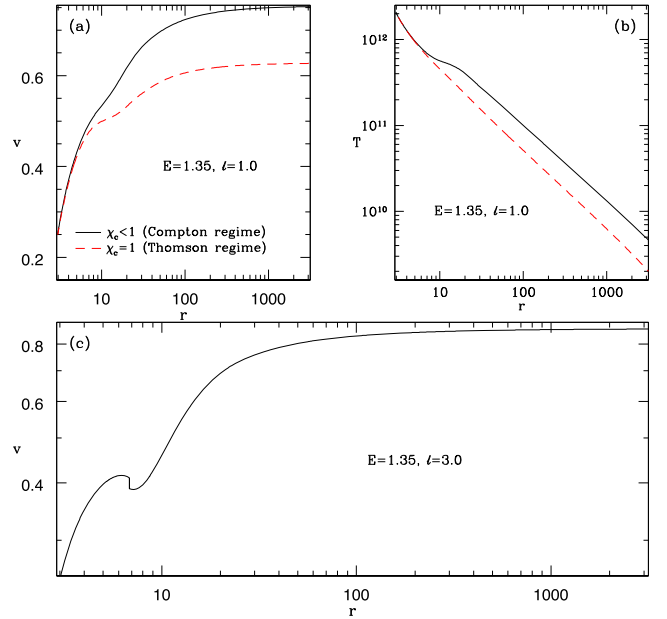

Figure 5. Nature of A-type solutions. Variation of (a) jet three-velocity v and (b) temperature T with r for $E = 1.35$ and $\ell = 1.0$. The solid curve incorporates Compton scattering, while the dashed curve considers Thomson scattering. (c) Variation of v for $\ell = 3.0$, $E = 1.35$.

sponds to certain jet base parameters like v_b and Θ_b. In Fig. 3, we plot E, for $e^- - p^+$ ($\xi = 1$) flow for different disc luminosities $\ell = 3.0$ (long dashed), 2.0 (solid), 1.0 (dotted) and 0.5 (dashed). The evolution of E indicates that higher ℓ makes the flow more energetic and E becomes non-monotonic. There are a couple of interesting features that separate the $E - r_c$ curve of this article from our previous ones (VC17; Vyas & Chattopadhyay 2018a; VC18b); these are as follows.

(i) E dips below one.

(ii) E dips up to a certain minimum value E_{min} and then another branch is obtained. Although the r_c at E_{min} is different for different luminosity, the energy is exactly the same.

In the next section, this phenomenon is discussed in detail.

4.3 General pattern of solutions and significance of Compton scattering

As E is a constant of motion, so Fig. 3 contains information about all types of jet solution. Each point on the figure corresponds to certain base variables v_b and Θ_b, corresponding to which there is a transonic solution. The solutions can be classified into three categories. To show their classification, we again plot the $E - r_c$ curve for $\ell = 1$ in Fig. 4. Three types of jet solution are named: A, B and C. The collective information for the base variables lies in the expression for E at the base, that is $E(r_b) = E_b = -h_b u_{tb} = h_b \sqrt{g_b^{rr}} \gamma_b$. In other words, the radiative contribution enters the Bernoulli expression as the jet propagates along r (equation 12). Interestingly, energy exchange between the jet and radiation allows even initially bound matter ($E < 1$) to be driven as transonic jets. This is a significantly different result in comparison with previous studies in the elastic scattering limit, where we were restricted to $E > 1$ for any transonic solution (see figure 6a of VC18b). We obtained this phenomenon previously in non-relativistic studies (Chattopadhyay & Chakrabarti 2000a,b), but such solutions were not systematically explored and the heating term was an ad hoc one.

Class A (w–x, dotted) and B (x–y, solid) in Fig. 4 represent sonic-point properties for jets starting with the same base (r_b). Type C (z–y, dashed) represents sonic-point properties of jets with the same ℓ but with $r_b > 3$. Class A represents high-energy jets and class B bound matter being driven off as jets starting with the same

r_b. Neither class B nor class C was obtained in the elastic scattering regime, i.e. with bound matter being driven out as jets. In addition, class C solutions are jet solutions of bound matter that is suspended at some height above the disc, while, for the B-class jets, $r_b = 3$ is similar to class A. At $r_b = 3$, the minimum energy of matter is obtained when $v_b \to 0$ and $\Theta_b \ll 1$, i. e.

$$E_{min} = \sqrt{g^{rr}}; \text{ i.e. } \gamma_b \to 1 \quad \text{ and } \quad h_b \to 1. \quad (16)$$

At E_{min}, B- and C-class solutions merge. It is precisely for this reason that $E - r_c$ reaches up to E_{min} for any ℓ (Figs 3 and 4). In the following, we discuss each class of solution separately.

4.4 A-type solutions: hot and fast jet base

In Fig. 5(a) and (b), we plot jet velocity v and temperature Θ as functions of r for $E = 1.35$ and $\ell = 1.0$. The jet in the Compton-
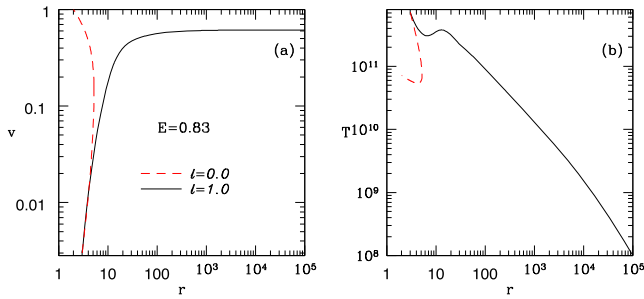
Figure 6. Nature of B-type solutions. Variation of (a) v and (b) T with r for $E = 0.83$ and $\ell = 1.0$ (solid) and $\ell = 0$ (dashed).

Figure 7. Minimum ℓ, i.e. $\ell_{\rm m}$, as a function of E for B-type solutions.

Figure 8. Nature of C-type solutions. Variation of (b) v and (c) T with r for $E = 0.63$ (solid) and $E = 0.92$ (dashed) for $\ell = 1.0$.

scattering regime has base velocity $v_{\rm b} = 0.14$ and base temperature $T_{\rm b} \sim 2 \times 10^{12}$ K. The sonic point is at $r = 5.97$, while terminal speed $v_{\rm t} = 0.69$. Here, terminal speeds are defined to be $v_{\rm t} = v|_{r \to 10^6}$. To show the effect of Compton scattering on the jet, we overplot the jet solution in the Compton-scattering regime (solid) with that in the Thomson-scattering one (dashed). The jet solution in the Thomson-scattering regime is achieved in the present formalism by considering $\chi_{\rm c} = 1$ and these jet solutions are similar to the ones obtained by VKMC15 and VC18b. The terminal speed of the jet in the Thomson-scattering regime is only 0.52. It is clear that the Compton-driven jet is 33 per cent faster compared with a jet under the Thomson-scattering regime. The temperature profile of the jet in the elastic scattering regime decreases monotonically, while temperature of the Compton jet is not monotonic, because the jet is heated up at around $r \sim 20$, where radiative moments peak (Fig. 2b). It cools down again monotonically with r, as the radiation field gets weaker further away. In Fig. 5(c), we plot v as a function of r of a jet with the same energy, i.e. $E = 1.35$; however, it is acted on by radiation characterized by $\ell = 3$. For these parameters, the jet accelerates and becomes transonic at the inner sonic point at $r_{\rm c} = 5.3$ and goes through shock transition under the impact of negative flux inside the funnel at $r = 6.3$. Through a shock discontinuity, the jet jumps from the supersonic branch to the subsonic branch and then again accelerates and becomes transonic at $r_{\rm c} = 8.62$, reaching a terminal speed $v_{\rm t} = 0.86$. The origin of generation of the shock, as well as the existence of multiple sonic points, lies in the radiation drag and negative flux inside the funnel (Fig. 2b dotted), which collectively resist the jet and form multiple sonic points. The details of the calculation of shock conditions are described in Vyas & Chattopadhyay (2018a; VC18b) and are not repeated here.

4.5 B-type solutions: hot and slow jet base

Class B solutions are bound solutions close to the horizon, i.e. $E < 1$ extending up to infinity driven by the radiation field (Fig. 4, solid). These solutions are characterized by low base speeds but high base temperature. In other words, the kinetic component of $E_{\rm b}$ is ineffective ($\gamma_{\rm b} \sim 1$). The thermal component is high ($h_{\rm b} > 1$) but dominated by gravity, $E \sim h_{\rm b} \sqrt{g_{\rm b}^{rr}} < 1$. Hence thermal driving by itself is unable to push matter outward (dashed) and it folds back on to the horizon, while the radiatively driven flow is transonic and escapes the gravity of the black hole. Matter is pushed outward collectively by radiation momentum deposition and energy transfer on to the jet. As these solutions are absent in the elastic scattering regime, Compton scattering is essential for driving jets with $E < 1$. We choose $E = 0.83$ and plot v and T with r in Fig. 6(a) and (b), respectively, for the choice of $\ell = 1$ (solid) and compare this with a thermally driven flow (i.e. a flow with $\ell = 0$: dashed). At $r_{\rm b} =$
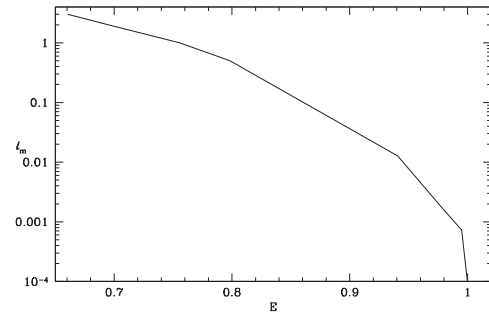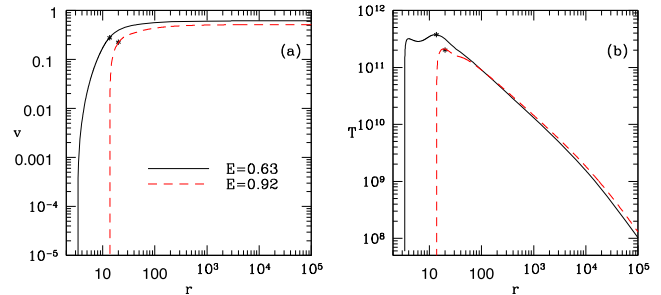
3, $v_{\rm b} = 0.003$ and $T_{\rm b} \sim 7 \times 10^{11}$ K for both flows, the radiatively driven jet (solid) flows to infinity through a sonic point $r_{\rm c} = 13.54$ and achieves a terminal speed $v_{\rm t} \sim 0.61$, but the thermally driven flow cannot expand to infinity against the gravity of the central black hole. This brings us to the question of what is the minimum disc luminosity required to blow a jet starting with specific energy $E < 1$. For $E > 1$ (i.e. A-type) jets, a transonic solution is guaranteed even for $\ell = 0$. As has been shown in Fig. 6(a) and (b) for B-type flows, a jet occurs if and only if $\ell > 0$. In Fig. 7, we plot the minimum disc luminosity $\ell_{\rm m}$ required to blow a transonic jet for B-type jets, i.e. as a function of E. For example, Fig. 7 shows that we can have transonic jet for $E < 0.75$ if the disc luminosity is $\ell > 1.0$.

4.6 C-type solutions: cold and very slow jet base

Solutions corresponding to the dashed line in the $E - r_{\rm c}$ plot (Fig. 4) attract special attention, as the jets represented by these solutions are characterized by $E < 1$ but, additionally, the bases of the jets are different and $r_{\rm b} > 3$. Therefore, for a given $r_{\rm b}$ and E, there is a maximum ℓ for which $v_{\rm b} \to 0$, so one can find jet solutions with the same E and ℓ if r_b is increased and these later solutions are the so-called C-type. Typically, the thermal ($T_{\rm b} << 10^{10}$) and kinetic ($v_{\rm b} \sim 0$) components of E at the jet base are very low. In Fig. 8(a)–(b), we plot v and T with r for $E = 0.63$ (solid) and $E = 0.92$ (dashed) and powered by disc radiation of $\ell = 1.0$. Both the jets are characterized by single sonic points (star marks) and the terminal speeds attained by both jets are around $v_{\rm t} \sim 0.6$. The base temperature and three-velocity are non-relativistic for both jets. The temperature profile of both jets rises from $T_{\rm b} \sim 10^7$ K to 3.7×10^{11} K (solid) and 2×10^{11} K (dashed) because of Compton heating. The base of the $E = 0.63$ jet is at $r_{\rm b} \gtrsim 3$, but for $E = 0.92$ it is at $r_{\rm b} = 12$, i.e. quite different, though they generate somewhat similar terminal quantities. The mechanism of heating and cooling can be understood if we look at equation (14). The first
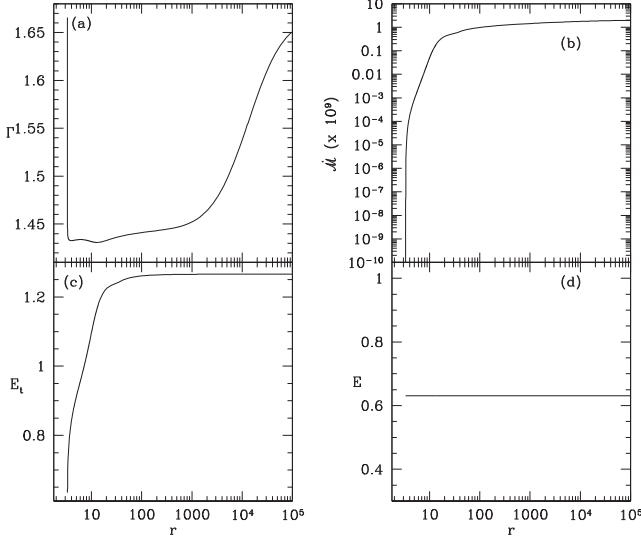
Figure 9. Variation of (a) Γ and (b) $\dot{\mathcal{M}}$, (c) E_t and (d) E for $E = 0.63$ (solid) and $\ell = 1.0$.

Figure 10. (a) Velocity profiles for various luminosities for C-type solutions for $e^- - p^+$ composition. Corresponding terminal speeds (v_t) are plotted in (b). (c) Variation of T with r for various luminosities. (d) Lorentz factor (γ_t) as a function of ℓ (solid). In panels (a) and (c), different curves are for $\ell = 3.0$ (solid), $\ell = 1.0$ (dotted) and $\ell = 0.5$ (dashed), keeping $E = 0.63$.

three terms inside the square bracket are positive and responsible for the decrease in jet temperature due to expansion. The last term in the bracket shows radiative heating. For $e^- - p^+$ flow, the heating term can be written as

$$Q^+ \approx (\Gamma - 1)(1 - \chi_c) \left[\frac{g^{rr}\mathcal{R}_0}{v} + \frac{v\mathcal{R}_2}{g^{rr}} - 2\mathcal{R}_1 \right]. \qquad (17)$$

At the base, $\Theta_b \approx v_b \approx$ small, moreover $\mathcal{R}_1 < 0$ inside the funnel, i.e. all the terms inside the bracket are positive and collectively heat up the jet near the base. In addition, since $v_b \sim$ small, then the first term within the parentheses of equation (17) is dominant and is responsible for the sharp rise in temperature at $r \sim r_b$. Interestingly, there is a second hump in the T profile of the jet. Within one Schwarzschild radius from the jet base, v increases by more than four orders of magnitude ($\sim 10^{-5} \sim \rightarrow 0.1$), so the first term tends to decrease, while the second term $v\mathcal{R}_2/g^{rr}$ starts to become important. The shape of the temperature profile is influenced by the relative strength of these two terms within the first few Schwarzschild radii from the base. If one studies the distribution of radiative moments carefully (Fig. 2a and b), then around $10 < r < 20$ the flux becomes positive, $R_1 > 0$, beyond which the third term $2R_1$ starts to dominate over both the first and second terms in parentheses in equation (17). This leads to a decrease in temperature and eventually the second peak. The first hump is therefore due to the first term in parentheses and the second is due to the interplay of all three terms, especially second and the third, although, for larger r, Compton heating is not important and the jet cools down due to expansion.

In Fig. 9(a)–(b), we plot the variation of Γ and $\dot{\mathcal{M}}$ corresponding to parameters of the jet corresponding to $E = 0.63$ in Fig. 8. Variation of Γ delivers similar information, in that the plasma is cold and non-relativistic at the base as well as far away ($r \sim 10^5$), but radiation makes it relativistic and hot in between. Variation of entropy depicts the non-adiabatic nature of the jet, as $\dot{\mathcal{M}}$ increases by around 10 orders of magnitude. As expected, E_t (Fig. 9c) evolves and increases due to the impact of radiation. Starting from $E_{tb} = 0.63$ (<1) at the base, it reaches at $E_t \sim 1.206$ (>1), while the generalized relativistic Bernoulli parameter E remains conserved and is shown to be a constant of motion (Fig. 9d).
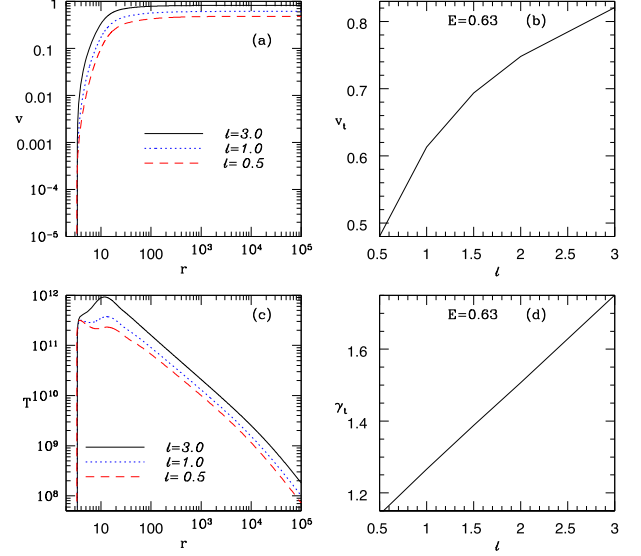
4.7 Effect of luminosity on C-type jet

We keep the same $E = 0.63$ and plot velocity profiles for $\ell = 3.0$ (solid), $\ell = 1.0$ (dotted) and $\ell = 0.5$ (dashed) in Fig. 10(a). As expected, greater acceleration is observed as the radiation field becomes more intense. To estimate the qualitative magnitude of acceleration and effect of ℓ, we plot v_T with ℓ for $E = 0.63$ in Fig. 10(b). Terminal speeds range from $v_t = 0.53$ to $v_t = 0.82$ as ℓ goes from 0.5 to 3.0.

The corresponding temperature profiles for these luminosities are shown in Fig. 10(c). Out of the two peaks, the first one is weakly dependent on ℓ, because it is mostly dictated by $v_b \rightarrow$ small (i.e. the first term in parentheses on the right-hand side of equation 17), while the second one depends on ℓ, because the second peak is born through the combined effect of all the moments.

4.8 Effect of composition on jet dynamics

Composition of relativistic jets is a much debated topic. Jets are believed to be dominated either by baryons ($e^- - p^+$ plasma) or by leptons (dominated by $e^- - e^+$). We have considered the relativistic EoS, which takes care of the composition of the plasma through ξ (Appendix A). It permits us to study the jet dynamics with variation of ξ. To study the effect of composition, we generate solutions by varying ξ for given values of E and ℓ. We plot three-velocity v in Fig. 11(a) and temperature T in Fig. 11(b) for $\xi = 1.0$ (solid) and $\xi = 0.05$ (dotted) for $E = 0.63$ and $\ell = 1.0$. As ξ decreases, the lepton fraction in the fluid composition increases, making the fluid lighter, hence the jet, under radiative acceleration, becomes faster. Corresponding terminal speeds are plotted in Fig. 11(c); these go up to 0.998 as the value of ξ drops to 0.05. In terms of terminal Lorentz factors γ_t of the jets (Fig. 11d), for very low $\xi (\sim 0.05)$, γ_t comfortably reaches up to 10. The temperature profiles of a baryon-dominated jet (solid) are mostly similar to those of lepton-dominated jets (dotted). For thermally driven jets or jets driven by radiation in the elastic scattering regime, the temperature
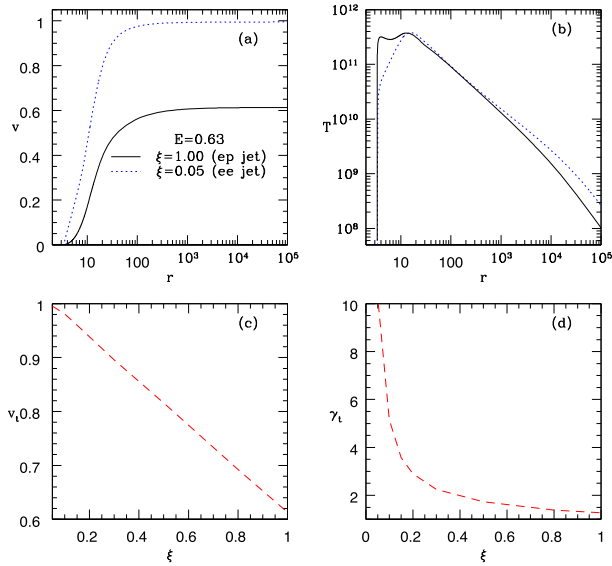
Figure 11. (a) v and (b) T profiles as a function of r for $\xi = 0.05$ (dotted) and $\xi = 1.00$ (solid). (c) v_t and (d) γ_t as a function of ξ. For all curves, $E = 0.63$ and $\ell = 1.0$.
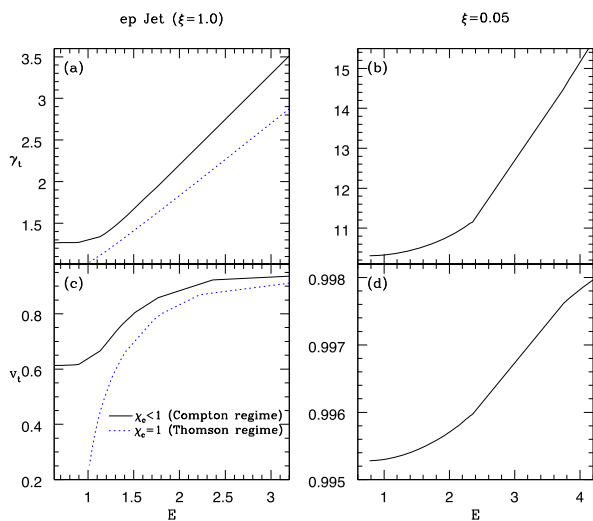

Figure 12. (a, b) Terminal Lorentz factor γ_t and (c, d) terminal speed v_t as a function of E. The composition of the jets is (a, c) $\xi = 1$ and (b, d) $\xi = 0.05$. The quantities in the Compton-scattering regime (solid) are compared with those in the Thomson-scattering regime (dotted) in panels (a) and (c). All the plots are for $\ell = 1.0$.

of baryon-dominated flows is greater than that of lepton-dominated ones; however, in the Compton-scattering regime, the energy transferred by radiation is more effective for flows with lower ξ (presence of ρ_e in the right-hand side of equation 8).

We plot γ_t and v_t with E for $\xi = 1.0$ (Fig. 12 a and c) and $\xi = 0.05$ (dashed; Fig. 12b and d). The curves are plotted for $\ell = 1.0$. For $e^- - p^+$ jets, we compare terminal quantities in the current article (solid) with those obtained in the Thomson-scattering regime (dotted, similar to VC18b), which reasserts the fact that Compton scattering accelerates jets more effectively than the Thomson regime. Further, as there are no solutions for $E < 1$ in the Thomson-scattering regime, the terminal speeds approach very low values as $E \to 1$. However, Compton-driven jets maintain $v_t > 0.6$ even for E

< 1. This lower limit of v_t or γ_t is highly relativistic ($v_t > 0.99$) for lepton-dominated jets (dashed). It may be noted that Fig. 11(a)–(d) is for C-type jets, but Fig. 12 represents all types of jet for given jet and radiative parameters.

5 DISCUSSION AND CONCLUDING REMARKS

In this article, we have studied radiatively driven relativistic jets in the Compton-scattering regime and curved space–time. The thermodynamics of the jet is described by a relativistic EoS. This work is a continuation of our previous efforts, where we studied the interaction between radiation and jet matter in the elastic scattering regime. In this article, we show that radiative driving in the Compton regime is significantly more effective than in the elastic scattering regime. In the Compton regime, both energy and momentum are transferred to the jet from the radiation field, so the radiation not only accelerates the flow but also increases its temperature. Consequently, we identified three classes or types of jet and named them A, B and C. Class A jets were those that are launched with very high temperatures and high speeds at the base with $E > 1$, class B are those that start with relatively lower speeds and temperatures and class C are those that have very low base temperatures and very small base speeds. Both B- and C-type jets have $E < 1$. This is because radiation transfers energy to matter, so that flows with $E < 1$ can also be ejected. In the scattering regime, at such E, the jet matter ejected outwards would actually fall back to the BH. The velocity distribution would almost overlap with the thermal one (dashed in Fig. 6a). For $E < 1$, the terminal Lorentz factors obtained for super-Eddington luminosities are below 2 for $e^- - p^+$ jets, but they are sufficiently high and reach beyond 10 for lepton-dominated jets. We reiterate that our previous articles (VKMC15; Vyas & Chattopadhyay 2018a; VC18b) had no counterpart of B- and C-type jets, because in the Thomson-scattering regime a transonic jet always has $E > 1$.

Astrophysical jets are transonic, fast and collimated and hence an assumption of conical or spherical jets is very common in theoretical investigations. If the jet was assumed to be adiabatic, then the assumption of a spherical jet is generally a fair one. However, in the Compton regime, radiation transfers energy to the jet, thereby heating it, so there are grounds for apprehension as to whether lateral expansion of the jet could destroy the spherical symmetry. In Appendix C, we show that, for transonic jets, the lateral expansion is much smaller than the radial expansion. In Fig. C1 we plot $\mathcal{K}$ as a function of r, where $\mathcal{K} = a_r/a_x$ or the ratio between radial acceleration and the lateral pressure gradient term. It is clear from the figure that $\mathcal{K} >$ a few, even in the subsonic region.

Radiatively driven jets possess multiple sonic points and internal shocks in a certain range of parameters. These internal shocks may be produced due to various factors. We showed in VC17 that a non-radial cross-section may harbour internal shocks. In Vyas & Chattopadhyay (2018a) and VC18b, we showed that, in the presence of radiation, even radial jets may undergo shock transitions. The shocks obtained in this article have similar features. A number of processes that give rise to internal shocks give theoretical support and strengthen the proposals that assumed internal shocks to explain various observed features of jets (Blandford & Königl 1979; Laurent et al. 2011), mainly the high-energy flux (GeV to TeV) of the radiation spectrum.

In this article, we have obtained jets with a variety of terminal speeds, ranging from mildly relativistic to highly relativistic. While jets in microquasars do show a range of terminal speeds, it is assumed that astrophysical jets are relativistic. Bulk speeds of the

jets are inferred from crude observational methods. However, the presence of asymmetry in the luminosity of a jet and its counterpart puts a better constraint on the estimation of Lorentz factors of jets (Wardle & Aaron 1997; Harris & Krawczynski 2006). The range of terminal Lorentz factors obtained in this article is similar to the ranges obtained for Lorentz factors in both X-ray binaries and AGN (Miller et al. 2006).

Quantitatively, we can conclude that, choosing a jet base at $r_b = 3$, $e^- - p^+$ jets can be accelerated to a minimum of of $v_t \sim 0.22$ for disc luminosity $\ell = 0.1$. For the same r_b and ℓ of lepton-dominated jets ($\xi = 0.1$), the minimum terminal speed is $v_t \sim 0.78$. Of course, for luminous discs ($\ell = 1$), terminal speeds for hot $e^- - p^+$ jets can go up to $v_t > 0.9$, while for lepton-dominated jets terminal Lorentz factors are ultrarelativistic.

REFERENCES

Beloborodov A. M., 2002, ApJ, 566, L85
Bini D., Geralico A., Jantzen R. T., Semerak O., 2015, MNRAS, 446, 2317
Blandford R. D., Königl A., 1979, ApJ, 232, 34
Buchler J. R., Yueh W. R., 1976, ApJ, 210, 440
Calvani M., Nobili L., 1982, Lettere al Nuovo Cimento, 35, 7
Chakrabarti S. K., 1989, ApJ, 347, 365
Chandrasekhar S., 1938, An Introduction to the Study of Stellar Structure. Dover, New York
Chattopadhyay I., 2005, MNRAS, 356, 145
Chattopadhyay I., 2008, in Chakrabarti S. K., Majumdar A. S., eds, AIP Conf. Ser. Vol. 1053, Proc. 2nd Kolkata Conf. on Observational Evidence of Black Holes in the Universe and the Satellite Meeting on Black Holes, Neutron Stars and Gamma-Ray Bursts. Am. Inst. Phys., New York, p. 353
Chattopadhyay I., Chakrabarti S. K., 2000a, Int. Journ. Mod. Phys. D, 9, 57
Chattopadhyay I., Chakrabarti S. K., 2000b, Int. Journ. Mod. Phys. D, 9, 717
Chattopadhyay I., Chakrabarti S. K., 2002a, MNRAS, 333, 454
Chattopadhyay I., Chakrabarti S. K., 2002b, Bulletin of the Astronomical Society of India, 30, 313
Chattopadhyay I., Das S., 2007, New Astron, 12, 454
Chattopadhyay I., Kumar R., 2016, MNRAS, 459, 3792
Chattopadhyay I., Ryu D., 2009, ApJ, 694, 492
Chattopadhyay I., Das S., Chakrabarti S. K., 2004, MNRAS, 348, 846
Curtis H. D., 1918, Lick Obs. Publ., 13, 31
Das S., Chattopadhyay I., Nandi A., Molteni D., 2014, 442, 251
Doeleman S. S. et al., 2012, Science, 338, 355
Fender R. P., Gallo E., Russell D., 2010, MNRAS, 406, 1425
Ferrari A., Trussoni E., Rosner R., Tsinganos K., 1985, ApJ, 294, 397
Fukue J., 1987, PASJ, 39, 309
Fukue J., 1996, PASJ, 48, 631
Fukue J., Tojyo M., Hirai Y., 2001, PASJ, 53, 555
Gallo E., Fender R. P., Pooley G. G., 2003, MNRAS, 344, 60
Harris D. E., Krawczynski H., 2006, ARA&A, 44, 463
Hsieh H. S., Spiegel E. A., 1976, ApJ, 207, 244
Icke V., 1989, A&A, 216, 294
Junor W., Biretta J. A., Livio M., 1999, Nature, 401, 891
Kato S., Fukue J., Mineshige S., 1998, Black-hole Accretion Disks. Kyoto Univ. Press, Kyoto
Kumar R., Chattopadhyay I., 2013, MNRAS, 430, 386
Kumar R., Chattopadhyay I., 2014, MNRAS, 443, 3444
Kumar R., Chattopadhyay I., 2017, MNRAS, 469, 4221
Kumar R., Singh C. B., Chattopadhyay I., Chakrabarti S. K., 2013, MNRAS, 436, 2864
Kumar R., Chattopadhyay I., Mandal S., 2014, MNRAS, 437, 2992
Laurent P., Rodriguez J., Wilms J., Bel M. C., Pottschmidt K., Grinberg V., 2011, Science, 332.6028, 438
Lee S.-J., Chattopadhyay I., Kumar R., Hyung S., Ryu D., 2016, ApJ, 831, 33
Mihalas D., Mihalas B. W., 1984, Foundations of Radiation Hydrodynamics. Oxford Univ. Press, Oxford
Miller J., James C. A., Fender R. P., Nakar E., 2006, MNRAS, 367.4, 1432
Molteni D., Ryu D., Chakrabarti S. K., 1996, ApJ, 470, 460
Narayan R., Kato S., Honma F., 1997, ApJ, 476, 49
Odell S. L., 1981, ApJ, 243, L147
Paczyński B., 1983, ApJ, 267, 315
Paczyński B., Wiita P. J., 1980, A&A, 88, 23
Park M. G., 2006, MNRAS, 367, 1739
Phinney E. S., 1982, MNRAS, 198, 1109
Pietrini P., Krolik J. H., 1995, ApJ, 447, 526
Quinn T., Paczynski B., 1985, ApJ, 289, 634
Rushton A., Spencer R., Fender R., Pooley G., 2010, A&A, 524, 29
Shakura N. I., Sunyaev R. A., 1973, A&A, 24, 337S
Sikora M., Wilson D. B., 1981, MNRAS, 197, 529
Singh K., Chattopadhyay I., 2018, MNRAS, 476, 4123
Synge J. L., 1957, The Relativistic Gas. Amsterdam, North Holland
Takahashi R., 2007, MNRAS, 382, 1041
Turolla R., Nobili L., Calvani M., 1986, ApJ, 303, 573
Vyas M. K., Chattopadhyay I., 2017, MNRAS, 469, 3270(VC17)
Vyas M. K., Chattopadhyay I., 2018b, A&A, 614, A51(VC18b)
Vyas M. K., Kumar R., Mandal S., Chattopadhyay I., 2015, MNRAS, 453, 2992(VKMC15)
Vyas M.K., Chattopadhyay I., 2018a, JA&A, 39, 12
Wardle J. F. C., Aaron S. E., 1997, MNRAS, 286, 425

APPENDIX A: RELATIVISTIC EQUATION OF STATE

At relativistic temperatures, the adiabatic index (Γ) depends upon temperature. The value of Γ ranges from 5/3 to 4/3 as the flow goes from non-relativistic temperatures to relativistic temperatures. We consider the EoS for multi-species, relativistic flow proposed by Chattopadhyay (2008) and Chattopadhyay & Ryu (2009), which is a close approximation of the exact relativistic EoS (Chandrasekhar 1938; Synge 1957; VKMC15). The EoS is given as

$$e = n_{e^-} m_e c^2 f, \text{ in physical dimensions,} \tag{A1}$$

where m_e and n_{e^-} are the rest mass of the electron and electron number density, respectively. f is a dimensionless quantity given by

$$f = (2 - \xi)\left[1 + \Theta\left(\frac{9\Theta + 3}{3\Theta + 2}\right)\right] + \xi\left[\frac{1}{\eta} + \Theta\left(\frac{9\Theta + 3/\eta}{3\Theta + 2/\eta}\right)\right]. \tag{A2}$$

Here, $\Theta = kT/(m_e c^2)$ is dimensionless temperature (T) and k is the Boltzmann constant. $\xi(= n_{p^+}/n_{e^-})$ is the ratio of number densities of protons and electrons. $\eta(= m_e/m_{p^+})$ is the mass ratio of electrons and protons. The expressions for Γ, N, a and h (in geometric units) are given by

$$N = \frac{1}{2}\frac{df}{d\Theta}, \Gamma = 1 + \frac{1}{N}, a^2 = \frac{\Gamma p}{e + p} = \frac{2\Gamma\Theta}{f + 2\Theta}, h = \frac{f + 2\Theta}{\tau} \tag{A3}$$

Here τ is a function of composition and is defined as $\tau = 2 - \xi + \xi/\eta$.

APPENDIX B: RADIATION FIELD FROM ACCRETION DISC AND ASSOCIATED RADIATION PARAMETERS

B1 Estimating approximate accretion-disc variables

Here, U^μ denotes the four-velocity components in the accretion disc and $v \equiv (\vartheta_x, 0, \vartheta_\phi)$ the corresponding three-velocity components

with x, θ, ϕ the spatial coordinates. $\vartheta = \vartheta_x / \sqrt{(1 - \vartheta_\phi^2)}$ is defined as the radial component of three-velocity measured by a local observer rotating along the disc surface. We can show the velocity distribution of the outer disc and the corona in the following compact form [see Appendix A of VKMC15]:

$$\vartheta_i = \left[1 - \frac{(x-2)x^2}{\{x^3 - [(x-2)\lambda^2]\}U_t^2|_{x_{0i}}} \right]^{1/2}. \tag{B1}$$

Here, the suffix i represents variables associated with the corona (i.e. i=C) and the outer disc (i.e. i=D). $U_t|_{x_{0i}}$ is the covariant time component of U^μ at the outer boundary of the respective disc components, which are $x_{0i} = x_{sh}$ and $x_{0i} = x_0$ for the corona and the outer disc, respectively. At x_0, $[\vartheta_D]_{x_0} \approx 0$ and it grows as it falls inwards.

The distribution of temperature can be obtained as (VKMC15)

$$\Theta_i = \Theta_0 \left(\frac{U_0^x x_{0i} H_0}{U_i^x x H_i} \right)^{\Gamma - 1}. \tag{B2}$$

The compression ratio R_c is defined as

$$R_c = U_-^r / U_+^r, \tag{B3}$$

where R_c is approximated from the results of Kumar & Chattopadhyay (2017):

$$R_c = 2.46 - 2.12 \times 10^{-3} x_{sh} - 4.72 \times 10^{-4} x_{sh}^2$$
$$+ 5.98 \times 10^{-6} x_{sh}^3 - 2.08 \times 10^{-8} x_{sh}^4. \tag{B4}$$

Similarly, the temperature increases by the same fraction R_c, giving the outer boundary velocity and temperature for the corona; using this in equations (B1) and (B2), ϑ_C and Θ_C are obtained.

Moreover, VKMC15 proposed a relation between x_{sh} and accretion rate $\dot{m}$, which, after converting into the current unit system, becomes

$$x_{sh} = 87.402 - 28.193\dot{m} + 3.125\dot{m}^2 - 0.115\dot{m}^3. \tag{B5}$$

x_{sh} is in geometric units, while $\dot{m}$ is the mass accretion rate in Eddington units (Eddington accretion rate is defined as $\equiv \dot{M}_{Edd} = 1.4 \times 10^{17} M_B/M_\odot \, \text{g s}^{-1}$). To specify ϑ_i and Θ_i at x, the local height H_i is also required. Following numerical simulations (Das et al. 2014; Lee et al. 2016), we define $H_0 = 0.4 H_{sh} + \tan \theta_D x_0$. Supplying the values of all parameters required, $[\vartheta_D]_{x_0}$, ρ_0, H_0 and $\dot{m}$ at the outer disc boundary, x_0, velocity, temperature and density values at all x_i, along with the location of x_{sh}, are obtained. The accretion parameters considered in this article are shown in Table B1.

Table B1. Disc parameters.

λ	x_0	$[\vartheta_D]_{x_0}$	$[\Theta_D]_{x_0}$	θ_D	H^*	d_0
3.6	$20000 r_S$	0.001	0.03	78.5º	40	$0.4 H_{sh}$

B2 Radiative intensity and luminosity from the accretion flow

Assuming a stochastic magnetic field in the accretion disc and considering that it is in partial equipartition with the gas pressure, we can assume that the ratio between the magnetic pressure (p_{mag}) and the gas pressure (p_{gas}) is a constant, β, i.e. $p_{mag} = B^2/8\pi = \beta p_{gas} = \beta n k T$. The outer disc emits through synchrotron and bremsstrahlung processes, while the corona additionally emits through the inverse-Compton process along with these. The frequency-integrated, local intensity for the outer disc is (Kumar & Chattopadhyay 2014;

VKMC15)

$$\tilde{I}_{i_0} = \tilde{I}_{syn} + \tilde{I}_{brem}$$
$$= \left[\frac{16}{3} \frac{e^2}{c} \left(\frac{e B_i}{m_e c} \right)^2 \Theta_i^2 n_i + 1.4 \times 10^{-27} n_i^2 g_b c \sqrt{\frac{\Theta_i m_e}{k}} \right]$$
$$\times \frac{(d_0 \sin \theta_i + x \cos \theta_i)}{3} \, \text{erg cm}^{-2} \, \text{s}^{-1}. \tag{B6}$$

Here, $x, n_i, \Theta_i, \theta_i, g_b(= 1 + 1.78\Theta_i^{1.34})$ and B_i are the radial distance, electron number density, local dimensionless temperature, semi-vertical angle, relativistic Gaunt factor and magnetic field, respectively, for both disc components. The factor multiplied outside the square brackets converts the emissivity (erg cm^{-3} s^{-1}) into intensity (erg cm^{-2} s^{-1}). Now, the emitted radiation from the outer disc is inverse-Comptonized within the disc; adding this, the specific intensity becomes (Pietrini & Krolik 1995; Buchler & Yueh 1976)

$$\tilde{I}_D = \tilde{I}_{D_0} \left(1 + 4\Theta_{De} + 16\Theta_{De}^2 \right)^{\tau_r + (\tau_r^2/3)}. \tag{B7}$$

Here, Θ_{De} is the dimensionless electron temperature of the outer disc component and τ_r is the optical depth, which depends on r and is found to be

$$\tau_r = \frac{K_0 \dot{m}}{u^r r h}, \tag{B8}$$

where

$$K_0 = \frac{1.44 \times 10^{17} \sigma_T c}{4 m_e (1 + 1/\eta) G \pi M_\odot}.$$

The outer disc luminosity is obtained by integrating $\tilde{I}_D$ over the whole disc surface, i.e.

$$L_D = 2 \int_{x_{sh}}^{x_0} \int_0^{2\pi} \tilde{I}_D r \left(1 - \frac{2}{r} \right)^2 \text{cosec}^2 \theta_D \, d\phi \, dx. \tag{B9}$$

Now, a fraction of radiation emitted from the outer disc falls on to the corona and adds to the radiation emitted by it and is calculated to be

$$L_D^f = 2 \int_{x_{sh}}^{x_0} \int_0^{2\pi} \tilde{I}_D r \left(1 - \frac{2}{r} \right)^2 \frac{1}{\pi} \tan^{-1} \left(\frac{x_{sh}}{x} \right)$$
$$\times \tan^{-1} \left(\frac{H_{sh}}{x} \right) \text{cosec}^2 \theta_D \, d\phi \, dx. \tag{B10}$$

Assuming that this radiation falls on to the corona homogeneously, we can calculate the additional specific intensity of the corona taking this radiation into account as

$$\tilde{I}_{C_0}^f = L_D^f / A_C. \tag{B11}$$

Including this radiation, along with local inverse Comptonization inside the corona, the coronal luminosity is obtained as

$$L_C = 2 \int_{x_{ii}}^{x_{sh}} \int_0^{2\pi} \left[\tilde{I}_{C_0} + \tilde{I}_{C_0}^f \right] \left(1 + 4\Theta_{Ce} + 16\Theta_{Ce}^2 \right)^{\tau_r + (\tau_r^2/3)}$$
$$\times r \left(1 - \frac{2}{r} \right)^2 \text{cosec}^2 \theta_C \, d\phi \, dx. \tag{B12}$$

Similarly, here Θ_{Ce} is the dimensionless electron temperature of the corona.

The above luminosities can be presented in units of $L_{Edd}(\equiv 1.38 \times 10^{38} M_B/M_\odot \, \text{erg s}^{-1})$ as $\ell_i = L_i/L_{Edd}$.

Considering the corona to be compact and having an isotropic distribution of radiation, we can formulate a relation for the specific

intensity of the corona in terms of L_C as

$$\tilde{I}_C = L_C/\pi A_C = \ell_C L_{Edd}/\pi A_C \ (\text{erg cm}^{-2} \, \text{s}^{-1}).$$ (B13)

B3 Radiative moments

B3.1 Relativistic transformation of intensities from various disc components

To solve the EoMs of the jet, we require information about the radiation field, governed by radiative moments on the jet axis. To obtain the radiative moments, we need to compute specific intensities from the outer disc as well as the corona. Using the expressions for velocity (B1) and temperature (B2) from both the disc components, we compute the radiative intensity (B6, B7, B11) in the local rest frame of the disc, which is transformed into the curved frame, following special and general relativistic transformations, as

$$I_i = \frac{\tilde{I}_i}{\gamma_i^4 \left[1 + \vartheta_j l^j\right]_i^4} \left(1 - \frac{2}{x}\right)^2,$$ (B14)

where $\tilde{I}_i$ is the frequency-integrated specific intensity in the local rest frame of the disc, ϑ^j is the jth component of three-velocity, γ_i being the Lorentz factor, and l^j are the direction cosines. The square of the redshift factor $(1 - 2/x)^2$ reduces radiation intensity close to the BH (Beloborodov 2002).

B3.2 Calculation of radiative moments in curved space–time

Zeroth, first and second moments of specific intensity (i.e. $\int I \, d\Omega$, $\int I l^j \, d\Omega$, ~ $\int I l^j l^k \, d\Omega$, respectively) contain all the information about the radiation field. There are 10 independent components (Mihalas & Mihalas 1984; Chattopadhyay 2005), but, to study a conical narrow jet passing through a radiation field, only three of these are dynamically important.

The radiative moments (R_0, R_1 and R_2) can be written in a compact form given by (Vyas & Chattopadhyay 2018a)

$$R_{ni} = \int_{x_{ii}}^{x_{i0}} \int_0^{2\pi} \left(1 - \frac{2}{x}\right)^3 \frac{\tilde{I}_i}{\gamma_i^4 \left[1 + v_j l^j\right]_i^4}$$

$$\times \left[\frac{(r - x\cos\theta_i)}{\sqrt{[(r - x\cos\theta_i)^2 + x^2 \sin^2\theta_i]}}\left(1 - \frac{2}{x}\right) + \frac{2}{x}\right]^n$$

$$\times \frac{rx \, d\phi \, dx}{[(r - x\cos\theta_i)^2 + x^2 \sin^2\theta_i]^{3/2}}.$$ (B15)

Here $i \to$ C and D signifies the contributions from the corona and outer disc, respectively. The integration is performed over x and ϕ, with the limits of integration being from x_{ii} (inner edge) to x_{i0} (outer edge) of the respective disc component and the angular circumference of the disc from 0 to 2π. The index $n = 0, 1, 2$ is for R_0, R_1 and R_2, which are the radiative energy density and radiative flux along r and rr components of the radiative pressure, respectively. θ is the semi-vertical angle of the respective disc component (Fig. 1).

$\gamma_i^4 \left[1 + v_j l^j\right]_i^4$ in the denominator inside the integration represents a special relativistic transformation of specific intensity (Chattopadhyay 2005), while $2/x$ accounts for the transformation of $\tilde{I}_i$, l^j and solid angle in curved space–time. These transformations are taken from methods developed by Beloborodov (2002) and Bini et al. (2015) and were used by Vyas & Chattopadhyay (2018a).
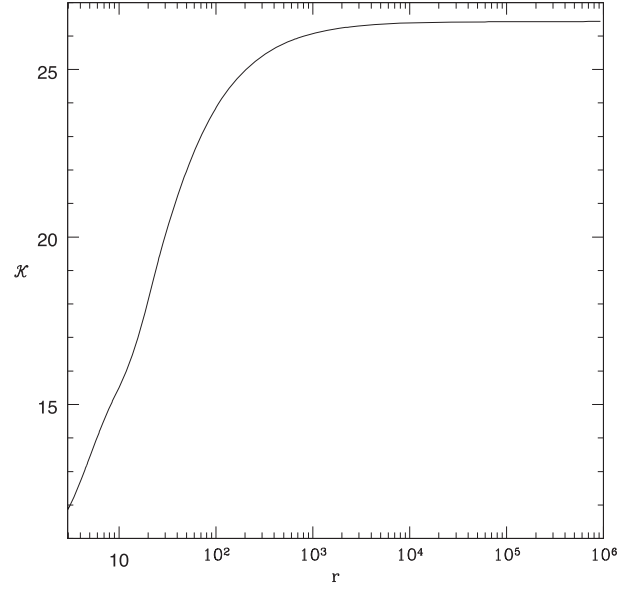

Figure C1. Variation of $\mathcal{K}$ with r for $\ell = 1$, $E = 1.35$.

As we have two disc components, corona and outer disc, the total moments are obtained as

$$R_n = R_{nC} + R_{nD}.$$ (B16)

The x limits for the corona are $x_{Ci} = 2$, $x_{C0} = x_{sh}$. Following the shading effect induced by the corona as it blocks a certain amount of radiation from the outer disc, the innermost edge seen from r is given by

$$x_{Di} = \frac{r - d_0}{(r - H_{sh})/x_{sh} + \cot\theta_C}.$$

It is clear from above that, as $r \to \infty$, $x_{Di} \to x_{sh}$. Further, up to some $r = r_{lim}$, radiation from the outer disc will not reach the jet axis. This limiting distance is obtained as

$$r_{lim} = \frac{x_0 H_{sh} - H_0 x_{sh}}{x_0 - x_{sh}}.$$ (B17)

APPENDIX C: ON VALIDITY OF THE SPHERICAL CROSS-SECTION OF THE JET

As radiation transfers energy to the jet matter, the jet heats up, increasing the pressure of the flow. The pressure gradient force, which is isotropic in the local frame, might compete with the radial expansion of the flow and the conical flow geometry of the jet may be compromised.

To justify this approximation, here we show that the outward acceleration of the jet is much more dominant over lateral expansion.

The jet acceleration along r is given by a_r (right-hand side of equation 5):

$$a_r = -\left(1 - \frac{2}{r} + u^r u^r\right)\frac{1}{e + p}\frac{dp}{dr} + \rho_e \frac{\sqrt{g^{rr}}\gamma^3}{(e + p)}\Im^r.$$ (C1)

Let $x = r\sin\alpha$ be the horizontal radius of the jet boundary and α the opening half-angle. Since α is small, therefore

$$\frac{dp}{dx} \approx \frac{dp}{dr}\frac{\delta r}{\delta x}.$$

Using the above expression, the horizontal pressure-gradient term can be written as

$$\frac{\mathrm{d}p}{\mathrm{d}x} \sim \frac{\mathrm{d}p}{\mathrm{d}r}\frac{\delta r}{\delta x} = \frac{(1 - \cos\alpha)}{\sin\alpha}\frac{\mathrm{d}p}{\mathrm{d}r}. \tag{C2}$$

This gradient of pressure from the jet axis to the jet wall leads to thermal expansion of the jet. Hence there is a net acceleration component of the jet away from the jet axis (call it a_x), which can be written as

$$a_x = -\left(1 - \frac{2}{r}\right)\frac{1}{e + p}\frac{\mathrm{d}p}{\mathrm{d}x} = -\left(1 - \frac{2}{r}\right)\frac{1}{e + p}\frac{(1 - \cos\alpha)}{\sin\alpha}\frac{\mathrm{d}p}{\mathrm{d}r}. \tag{C3}$$

Now, to compare a_r and a_x, we define

$$\mathcal{K} = \frac{a_r}{a_x}. \tag{C4}$$

If $\mathcal{K} \lesssim 1$, then the assumption of conical flow geometry will not hold. To analyse this, we choose $\alpha = 10°$ and take an example of an A-type solution (Fig. 5), for $\ell = 1$ and $E = 1.35$, and plot $\mathcal{K}$. The variation of $\mathcal{K}$ is shown in Fig. C1.

We see that $\mathcal{K}$ remains significantly greater than 1 throughout the jet extent and increases with r. Hence we can safely state that the assumption of conical flow geometry is a reasonable one.

This paper has been typeset from a TeX/LaTeX file prepared by the author.